



2013-06

Bi-material terahertz sensors using metamaterial structures

Alves, Fabio

<http://hdl.handle.net/10945/44106>



Calhoun is a project of the Dudley Knox Library at NPS, furthering the precepts and goals of open government and government transparency. All information contained herein has been approved for release by the NPS Public Affairs Officer.

**Dudley Knox Library / Naval Postgraduate School
411 Dyer Road / 1 University Circle
Monterey, California USA 93943**

<http://www.nps.edu/library>

Bi-material terahertz sensors using metamaterial structures

Fabio Alves,^{1,*} Dragoslav Grbovic,¹ Brian Kearney,¹
Nickolay V. Lavrik,² and Gamani Karunasiri¹

¹Department of Physics, Naval Postgraduate School, 833 Dyer Rd, Monterey, CA 93943, USA
²Center for Nanophase Materials Science, Oak Ridge National Laboratory, Oak Ridge, TN 37831, USA
[*fdalves@nps.edu](mailto:fdalves@nps.edu)

Abstract: In this paper we report on the design, fabrication and characterization of terahertz (THz) bi-material sensors with metamaterial absorbers. MEMS fabrication-friendly SiO_x and Al are used to maximize the bimetallic effect and metamaterial absorption at 3.8 THz, the frequency of a quantum cascade laser illumination source. Sensors with different configurations were fabricated and the measured absorption is near 100% and responsivity is around 1.2 deg/μW, which agree well with finite element simulations. The results indicate the potential of using these detectors to fabricate focal plane arrays for real time THz imaging.

©2013 Optical Society of America

OCIS codes: (040.2235) Far infrared or terahertz; (160.3918) Metamaterials.

References and links

1. J. F. Federici, B. Schulkin, F. Huang, D. Gary, R. Barat, F. Oliveira, and D. Zimdars, "THz imaging and sensing for security applications—explosives, weapons, and drugs," *Semicond. Sci. Technol.* **20**(7), S266–S280 (2005).
2. S. M. Kim, F. Hatami, J. S. Harris, A. W. Kurian, J. Ford, D. King, G. Scalari, M. Giovannini, N. Hoyler, J. Faist, and G. Harris, "Biomedical terahertz imaging with a quantum cascade laser," *Appl. Phys. Lett.* **88**(15), 153903 (2006).
3. Z. D. Taylor, R. S. Singh, M. O. Culjat, J. Y. Suen, W. S. Grundfest, H. Lee, and E. R. Brown, "Reflective terahertz imaging of porcine skin burns," *Opt. Lett.* **33**(11), 1258–1260 (2008).
4. J. E. Bjarnason, T. L. J. Chan, A. W. M. Lee, M. A. Celis, and E. R. Brown, "Millimeter-wave, terahertz, and midinfrared transmission through common clothing," *Appl. Phys. Lett.* **85**(4), 519–521 (2004).
5. R. H. Clothier and N. Bourne, "Effects of THz exposure on human primary keratinocyte differentiation and viability," *J. Biol. Phys.* **29**(2/3), 179–185 (2003).
6. A. W. M. Lee, B. S. Wil, S. Kumar, Qing Hu, and J. L. Reno, "Real-time imaging Using a 4.3-THz quantum cascade laser and a 320x240 microbolometer focal-plane array," *IEEE Photon. Technol. Lett.* **18**(13), 1415–1417 (2006).
7. B. N. Behnken, G. Karunasiri, D. R. Chamberlin, P. R. Robrish, and J. Faist, "Real-time imaging using a 2.8 THz quantum cascade laser and uncooled infrared microbolometer camera," *Opt. Lett.* **33**(5), 440–442 (2008).
8. D. Grbovic, N. V. Lavrik, S. Rajic, and P. G. Datskos, "Arrays of SiO₂ substrate-free micromechanical uncooled infrared and terahertz detectors," *J. Appl. Phys.* **104**(5), 054508 (2008).
9. B. Su and G. Duan, "A High sensitivity THz detector," *Proc. SPIE* **8195**, 81951K (2011).
10. X. Liu, B. Wang, X. Lu, E. Liang, and G. Yang, "Far infrared/terahertz micromechanical imaging-array sensors based on nano-scale optical measurement technology," *Proc. SPIE* **7204**, 720403 (2011).
11. G. P. Berman, B. M. Chenobrod, A. R. Bilhop, and V. Gorshkov, "Uncooled infrared and terahertz detectors based on micromechanical mirror as a radiation pressure sensor," *Proc. SPIE* **8195**, 819518 (2011).
12. J. Hastanin, Y. Renotte, K. Fleury-Frenette, J. M. Defise, and S. Habraken, "A far infrared/terahertz micromechanical sensor based on surface plasmons resonance," *Proc. SPIE* **7113**, 71131C, 71131C-9 (2008).
13. S. Timoshenko, "Analysis of bi-metal thermostat," *J. Opt. Soc. Am.* **11**(3), 233–255 (1925).
14. J. A. Harkey and T. W. Kenny, "1/f noise considerations for the design and process optimization of piezoresistive cantilevers," *J. Microelectromech. Syst.* **9**(2), 226–235 (2000).
15. S. R. Hunter, R. A. Amantea, L. A. Goodman, D. B. Kharas, S. Gershtein, J. R. Matey, S. N. Perna, Y. Yu, N. Maley, and L. K. White, "High-sensitivity uncooled microcantilever infrared imaging arrays," *Proc. SPIE* **5074**, 469–480 (2003).
16. J. Wu, G. K. Fedder, and L. R. Carley, "A low-noise low-offset capacitive sensing amplifier for a 50- $\sqrt{\text{g/Hz}}$ monolithic CMOS MEMS accelerometer," *IEEE J. Sol. Stat. Circ.* **39**(5), 722–730 (2004).
17. Q. Zhang, Z. Miao, Z. Guo, F. Dong, Z. Xiong, X. Wu, D. Chen, C. Li, and B. Jiao, "Optical readout uncooled infrared imaging detector using knife-edge filter operation," *Optoelec. Lett.* **3**(2), 119–122 (2007).

18. T. Cheng, Q. Zhang, B. Jiao, D. Chen, and X. Wu, "Optical readout sensitivity of deformed microreflector for uncooled infrared detector: theoretical model and experimental validation," *J. Opt. Soc. Am. A* **26**(11), 2353–2361 (2009).
19. T. Perazzo, M. Mao, O. Kwon, A. Majumdar, J. B. Varesi, and P. Norton, "Infrared vision uncooled micro-optomechanical camera," *Appl. Phys. Lett.* **74**(23), 3567–3569 (1999).
20. S. Hunter, G. Maurer, G. Simelgor, S. Radhakrishnan, and J. Gray, "High sensitivity 25 μ m and 50 μ m pitch microcantilever IR imaging arrays," *Proc. SPIE* **6542**, 65421F, 65421F-13 (2007).
21. Y. Zhao, M. Y. Mao, and R. Horowitz, "Optomechanical uncooled infrared imaging system: Design, microfabrication, and performance," *J. Microelectromech. Syst.* **11**(2), 136–146 (2002).
22. F. Dong, Q. Zhang, D. Chen, L. Pan, Z. Guo, W. Wang, Z. Duan, and X. Wu, "An uncooled optically readable infrared imaging detector," *Sens. Actuators A Phys.* **133**(1), 236–242 (2007).
23. H. T. Chen, J. F. O'Hara, A. K. Azad, and A. J. Taylor, "Manipulation of terahertz radiation using metamaterials," *Laser Phot. Rev.* **5**(4), 513–533 (2011).
24. Y. Ma, Q. Chen, J. Grant, S. C. Saha, A. Khalid, and D. R. S. Cumming, "A terahertz polarization insensitive dual band metamaterial absorber," *Opt. Lett.* **36**(6), 945–947 (2011).
25. H. Luo, Y. Z. Cheng, and R. Z. Gong, "Numerical study of metamaterial absorber and extending absorbance bandwidth based on multi-square patches," *Eur. Phys. J. B* **81**(4), 387–392 (2011).
26. H. Tao, E. A. Kadlec, A. C. Strikwerda, K. Fan, W. J. Padilla, R. D. Averitt, E. A. Shaner, and X. Zhang, "Microwave and Terahertz wave sensing with metamaterials," *Opt. Express* **19**(22), 21620–21626 (2011).
27. F. Alves, B. Kearney, D. Grbovic, N. V. Lavrik, and G. Karunasiri, "Strong terahertz absorption using SiO₂/Al based metamaterial structures," *Appl. Phys. Lett.* **100**(11), 111104 (2012).
28. F. Alves, D. Grbovic, B. Kearney, and G. Karunasiri, "Microelectromechanical systems bi-material Terahertz Sensor with Integrated Metamaterial Absorber," *Opt. Lett.* **37**(11), 1886–1888 (2012).
29. Z. Djuric, D. Randjelovic, I. Jokic, J. Matovic, and J. Lamovecet, "A new approach to IR bimaterial detectors theory," *Infrared Phys. Technol.* **50**(1), 51–57 (2007).
30. P. W. Kruse, "Uncooled Infrared Imaging Arrays and Systems," in *Semiconductors and Semimetals 47: Uncooled Infrared Imaging Arrays and Systems*, P. W. Kruse and D.D. Skatrud, ed. (Academic Press, 1997).
31. P. G. Datskos, N. V. Lavrik, and S. Rajic, "Performance of uncooled microcantilever thermal detectors," *Rev. Sci. Instrum.* **75**(4), 1134–1148 (2004).
32. E. L. Dereniak and G. D. Boreman, *Infrared Detectors and Systems* (Wiley, 1996).
33. P. W. Kruse, *Uncooled Thermal Imaging, Arrays Systems and Applications* (SPIE Press, 2002).
34. Z. Y. Hu, T. Thundat, and R. J. Warmack, "Investigation of adsorption and absorption-induced stresses using microcantilever sensors," *J. Appl. Phys.* **90**(1), 427–431 (2001).
35. D. Briggs, Center for Nanophase Materials Sciences, Oak Ridge National Laboratory, Oak Ridge, TN, 37831 (personal communication, 2012).
36. B. Kearney, F. Alves, D. Grbovic, and G. Karunasiri, "Al/SiO₂/Al single and multiband metamaterial absorbers for terahertz sensor applications," *Opt. Eng.* **52**(1), 013801 (2013).
37. H. Tao, N. I. Landy, C. M. Bingham, X. Zhang, R. D. Averitt, and W. J. Padilla, "A metamaterial absorber for the terahertz regime: Design, fabrication and characterization," *Opt. Express* **16**(10), 7181–7188 (2008).
38. H.-T. Chen, "Interference theory of metamaterial perfect absorbers," *Opt. Express* **20**(7), 7165–7172 (2012).
39. Q. Y. Wen, Y. S. Xie, H. W. Zhang, Q. H. Yang, Y. X. Li, and Y. L. Liu, "Transmission line model and fields analysis of metamaterial absorber in the terahertz band," *Opt. Express* **17**(22), 20256–20265 (2009).
40. D. Y. Shchegolkov, A. K. Azad, J. F. O'Hara, and E. I. Simakov, "Perfect subwavelength fishnet like metamaterial-based film terahertz absorbers," *Phys. Rev. B* **82**(20), 205117 (2010).
41. H.-T. Chen, J. Zhou, J. F. O'Hara, F. Chen, A. K. Azad, and A. J. Taylor, "Antireflection coating using metamaterials and identification of its mechanism," *Phys. Rev. Lett.* **105**(7), 073901 (2010).
42. T. Maier and H. Brückl, "Wavelength-tunable microbolometers with metamaterial absorbers," *Opt. Lett.* **34**(19), 3012–3014 (2009).
43. J. Hao, L. Zhou, and M. Qiu, "Nearly total absorption of light and heat generation by plasmonic metamaterials," *Phys. Rev. B* **83**(16), 165107 (2011).
44. S. Fatholouloumi, D. Ban, H. Luo, E. Dupont, S. R. Laframboise, A. Boucherif, and H. C. Liu, "Thermal behavior investigation of terahertz quantum-cascade lasers," *IEEE J. Quantum Electron.* **44**(12), 1139–1144 (2008).

1. Introduction

Imaging with terahertz (THz) radiation is attractive for security [1] and medical [2, 3] applications due to its ability to penetrate most dry, non-metallic, non-polar materials without damaging them while resolving details that could be concealed in another spectral range, such as skin features and metallic objects [1–5]. Real-time THz imaging has been demonstrated using conventional, microbolometer-based imagers optimized for infrared (IR) wavelengths (8–12 μ m) coupled with a quantum cascade laser (QCL) as an illumination source [6, 7]. The limitations of this approach are the low sensitivity of the microbolometer cameras in the THz

region and small pixel size ($\sim 30 \mu\text{m}$), compared with THz wavelengths ($\sim 100 \mu\text{m}$ at 3 THz). One potential approach for efficient THz imaging is the use of bi-material detectors [8–12].

A typical bi-material detector (see Fig. 1(a)) consists of a sensing element (absorber) responsible for converting incoming radiation to heat which is transmitted by conduction to two symmetrically located bi-material beams (bi-material legs) connected to the host substrate (heat sink) by supporting structures of lower thermal conductance (anchors). The bi-material legs undergo bimetallic deformation [13] due to the temperature rise upon absorption of incident radiation. The deformation can be probed by different approaches such as piezoresistive [14], capacitive [15, 16] and optical readouts [8, 12, 17, 18]. The latter requires a reflective surface, normally embedded into the absorber, and has the advantage of avoiding the complex on-chip integrated microelectronics necessary for other approaches. Several bi-material based sensors have been demonstrated for IR detection and imaging [8, 19–22]. These detectors either use IR sensitive structural materials such as SiN_x and SiO_2 or, alternatively, integrate separate IR sensitive layers into the detector. Additional difficulties exist when the detection range is extended to the THz region. The low thermal background power in THz demands highly sensitive detectors and, in most cases, external THz illumination is also required [7–12]. The lack of fabrication-friendly natural materials exhibiting high THz absorption makes metamaterial absorbers tuned to THz frequencies very attractive.

Several groups have reported results on metamaterial structures operating in THz spectral band using a variety of configurations, including split-ring resonators and periodic arrays of metallic squares and rings [23–27]. A recent work demonstrated a micromechanical sensor operating in microwave and sub-terahertz frequencies using a single split-ring resonator with simulated absorption of around 40% [26]. Our group has recently demonstrated the ability to integrate highly absorbing metamaterial films into bi-material sensors. Our preliminary results, reported in [28], showed that this combined configuration has great potential in THz sensing and imaging. In this article, we report, in detail, the design, fabrication, and characterization of highly sensitive micromechanical bi-material THz detectors based on metamaterial structures. Initial work on imaging of a THz-QCL beam using a detector array is also included.

2. Bi-material sensors

For imaging applications, the most important sensor characteristics are high responsivity, fast operation and low noise. In thermal detectors, sensitivity and speed are controlled by heat capacitance (C) and thermal conductance (G) of the sensor in addition to the efficiency of absorption of incident radiation. Detectors are typically designed to have thermal conductance close to that of via radiation losses. Heat loss due to convection is dependent on the pressure of the surrounding gas [29] and can be minimized by operating the detectors at a relatively low pressure.

Solving the heat balance equation under incident radiation modulated at frequency ω yields [30]:

$$dT = \frac{\eta P_0}{G\sqrt{1 + \omega^2 \tau^2}}, \quad (1)$$

where, dT is the amplitude of temperature change of the sensor, P_0 is the amplitude of the incident power, η represents the fraction of incident power absorbed by the sensor, and $\tau (= C/G)$ is the thermal time constant. The responsivity (R) of a bi-material sensor can be defined as angular deflection per unit incident power ($d\theta/dP$), which is given by:

$$\frac{d\theta}{dP} = \frac{\eta}{G\sqrt{1 + \omega^2 \tau^2}} \frac{d\theta}{dT}, \quad (2)$$

where, $d\theta/dT$ is the angular deflection per unit temperature (thermomechanical sensitivity). The speed of the sensor is primarily limited by the thermal time constant [8]. Noise in bi-material sensors arises from several different sources such as temperature fluctuations, background fluctuations, thermo-mechanical resonances, illumination source fluctuations and the readout system [31]. The first four manifest as fluctuations in the overall sensor deflection, while the readout noise depends on the probing mechanism. In a practical sense, the total noise of the complete detection system can be described by the noise equivalent power (NEP). For bi-material sensors, NEP can be defined as the incident radiant power that produces an angular deflection equal to detector's root mean square (rms) noise [32, 33].

Fundamentally, there are two main choices when designing a bi-material sensor: materials and configuration. Materials should be fabrication-friendly, exhibit low residual stress, have very different thermal expansion coefficients and strong THz absorption. Configurations should have a large absorption area, good thermal isolation to increase sensitivity, and provide a reflective surface for optical readout. All of these requirements are intrinsically interdependent making the optimization of the final sensor highly dependent on the intended application. Nonetheless, the quest to achieve high performance THz bi-material detectors starts with $d\theta/dT$, defined by the bimetallic effect, and η , which is maximized by the integration of metamaterial structures. In our previous work [28] a complex configuration of two fourfold legs metalized in opposite sides were used. Although the total length, and thus bi-material effect, was twice that of the current design (see Fig. 1(a)), the THz sensitive area was half the size to keep the overall pixel size around $200 \times 200 \mu\text{m}^2$. The metallization of the front and back sides of alternate legs caused the structure to be highly stressed after release. As a result, the sensors were bent as much as 30 degrees out of the substrate plane, which is problematic for the optical readout. The configuration reported here exhibits several advantages, which are highlighted in the next sections.

To increase sensitivity, it is important to optimize the bi-material layer thickness to maximize the deflection under increasing temperature. The linear displacement (Δz_{leg}) of the free tip of a bi-material beam, as depicted in Fig. 1(b), was first quantified by Timoshenko [13] and further explored by other groups [31, 34]. If the linear displacement is much smaller than the length of the bi-material beam (l_b), which is true in our case, the angular deflection due to temperature change ($d\theta/dT$) or thermomechanical sensitivity can be estimated using:

$$\frac{d\theta}{dT} = 6l_b (t_1 + t_2)t_2^{-2} \left(4 + 6\frac{t_1}{t_2} + 4\frac{t_1^2}{t_2^2} + \frac{t_1^3}{t_2^3} \frac{E_1}{E_2} + \frac{t_2}{t_1} \frac{E_2}{E_1} \right)^{-1} (\alpha_1 - \alpha_2), \quad (3)$$

where t represents thickness, α is the thermal expansion coefficient and E is the Young's modulus. The indices 1 and 2 are used to represent materials 1 and 2, respectively.

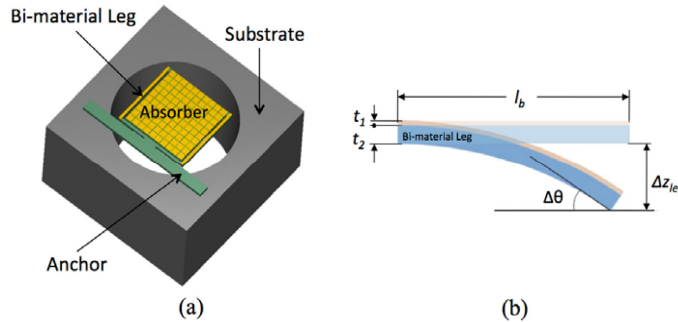


Fig. 1. Bi-material sensor. (a) 3D view of the THz bi-material sensor with metamaterial absorber, fabricated on a Si substrate. (b) Close up of an isolated bi-material beam which length is l_b , and metal and dielectric thickness t_1 and t_2 respectively. Δz_{leg} and $\Delta\theta$ are the linear and angular deflection of the beam, respectively.

When the bi-material legs are connected to a freestanding flat absorber (see Fig. 2(a)), the sensor angular deflection is approximately equal to $\Delta\theta$ (see Fig. 1(b)). The effect can be further amplified by adding multifold legs with alternate bi-material segments [28]. However, such a configuration also magnifies the bending due to residual stress after release. Table 1 lists some of the most common MEMS materials along with their structural, thermal and electrical characteristics.

Table 1. Properties of standard MEMS materials^a.

Material	Young's Modulus $E (\times 10^6 \text{ Pa})$	Expansion Coefficient $\alpha (\times 10^{-6} \text{ K}^{-1})$	Thermal Conductivity $\kappa (\text{Wm}^{-1}\text{K}^{-1})$	Heat Capacity $c (\text{J kg}^{-1} \text{ K}^{-1})$	Density $\rho (\times 10^{-3} \text{ kg m}^{-3})$	Electric Conductivity $\sigma (\times 10^6 \text{ S m}^{-1})$	THz refractive index ^b n^*
Si	100	2.7	130	750	2330	—	3.48-0.01i
SiN _x	180	2.1	19	691	2400	—	2.1-0.025i
SiO ₂	68	0.4	1.4	703	2200	—	2.0-0.02i
Al	70	25	237	900	2700	10	—
Au	77	14.2	296	129	19300	37	—

^aFrom J. App. Phys. **104**(5), 054508 (2008).

^bFrom App. Opt. **46**(33), 8818-8813 (2007).

Figure 2(b) shows the angular deformation calculated using Eq. (3) for the structure depicted in Fig. 2(a) for different combinations of metal/dielectric in Table 1, where the length of the leg is fixed to 214 μm , the dielectric thickness is kept constant at 1.1 μm and the metal thickness is varied from 10 to 800 nm. Finite element (FE) simulation and experimental results for $t_1 = 170$ nm show that the analytical model slightly underestimates the bimetallic effect (circular marker in Fig. 2(b)) for this specific configuration.

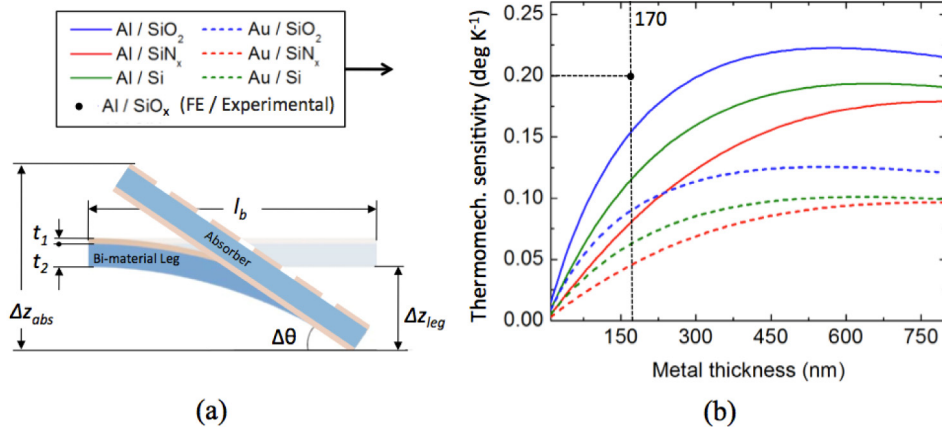


Fig. 2. Thermomechanical deflection of the bi-material sensor. (a) Freestanding flat THz absorber connected to a bi-material beam, whose length is l_b , and metal and dielectric thickness t_1 and t_2 respectively. Δz_{abs} is the total linear displacement and $\Delta\theta$ is the angular deflection of the absorber. (b) Thermomechanical sensitivity ($d\theta/dT$) of the structure of part (a), calculated using (3) for all combinations of metal/dielectric of Table 1 where t_1 varies from 10 to 800 nm and t_2 is fixed in 1.1 μm . The circular marker shows FE and experimental results for $t_1 = 170$ nm.

It is clear from Fig. 2 that the Al/SiO₂ combination produces the highest sensitivity with the maximum occurring when the metal thickness is approximately one-half of the dielectric thickness. Non-stoichiometric SiN_x can provide less stressed layers than SiO₂ [35], however, silicon-rich SiO_x can be deposited with much lower stress than SiO₂, while preserving most of the thermomechanical and electro-optical properties. During sensor fabrication, testing layers

of non-stoichiometric SiO_x and stoichiometric SiO_2 layers with the same thickness were deposited on Si substrates with intrinsic stress on the order of -13 MPa and -140 MPa, respectively. By selecting SiO_x and Al (both standard MEMS materials), it is possible to maximize $d\theta/dT$ while simultaneously alleviating some of the excessive residual stress related deformation observed in the sensors fabricated in [28]. Furthermore, SiO_x and Al exhibit electro-optical properties that are suitable for highly efficient metamaterial absorbers, discussed in the following section.

4. Metamaterial absorber for THz frequencies

The ability of metamaterials to exhibit absorption characteristics not found in their constituents makes them attractive for fabricating absorbers to integrate into bi-material sensors. With the proper structural parameters, a “perfect” absorber can be constructed for specific narrow band of frequencies [27, 36]. The challenge is to design a metamaterial film thin enough to provide low thermal capacitance (to not degrade the thermal time constant), while providing structural strength, low stress, and a flat reflective surface for an optical readout. A metamaterial absorber can be designed using a periodic array of Al square elements separated from an Al ground plane by a SiO_x layer, as schematically illustrated in Fig. 3(a) for a single unit cell. Such a combination allows matching to the free space impedance at specific frequencies, eliminating the reflection, while the ground plane prevents transmission, resulting in nearly 100% absorption. Figure 3(b) shows a fabricated metamaterial structure on a Si substrate [36].

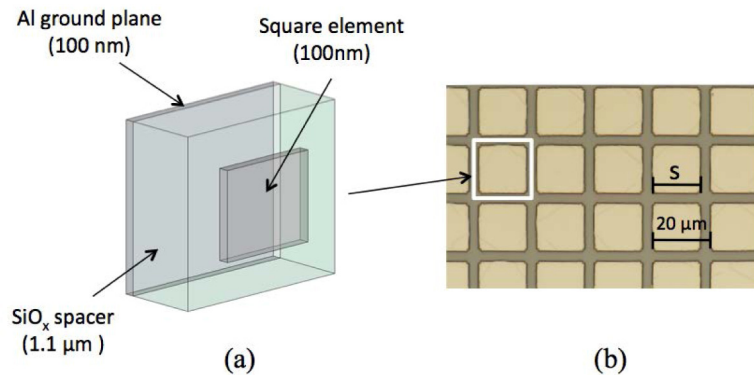


Fig. 3. Metamaterial absorber. (a) Schematics of a metamaterial unit cell of a periodic array of Al square elements separated from an Al ground plane by a SiO_x layer. (b) Metamaterial test structures with 20 μm period and varying square dimension (s), fabricated in a Si substrate [36].

It is known that for these structures the peak absorption frequency depends on the inverse of the size of the aluminum squares (s) [36]. The explanation of this phenomenon is still under debate and there are different theoretical approaches. The physical mechanism of the absorption effect has been explained by the excitation of localized electromagnetic resonances, especially the magnetic resonance, evidenced by the anti-parallel surface currents excited in the two metallic layers [37]. On the other hand, investigation using interference models have shown that the anti-parallel surface currents are reproduced by interference and superposition and there is no magnetic coupling between the top and bottom metallic layers [38]. In addition, transmission line [39], cavity resonance [40] and Fabry-Pérot resonance [41] models have also been proposed. Qualitatively, the interaction of electromagnetic radiation with a metamaterial structure can be described using an equivalent LRC resonator circuit [42] with resonant frequency ($=1/\sqrt{LC}$). Since the capacitance depends on s^2 , an

inverse linear dependence on size is expected for the resonant frequency, which agrees with the experimental observations [36].

The relatively complex nature of metamaterial structures makes numerical simulations, generally, the preferred modeling method. The design of the metamaterial structures was performed by finite element (FE) modeling using COMSOL multiphysics software. The periodic nature of the metamaterial structures allows the simulation to be performed in a unit cell with the appropriate boundary conditions. The COMSOL radio frequency (RF) module allows an incident plane wave of THz radiation with a given intensity and propagation direction to penetrate a surface using scattering conditions or be generated on a boundary using ports. To simulate a unit cell, the configuration shown in Fig. 4(a) was used. Domains other than metal or dielectric were assumed to be free space. Perfect electric conductors (PEC) and perfect magnetic conductors (PMC) were used as periodic boundary conditions for normally incident radiation while Floquet boundary conditions can be used for oblique incidence [27, 36]. The combination of the active port (1) and the passive port (2) allows the scattering parameters in the structure to be determined from which the reflection ($R = |S_{11}|^2$) and transmission ($T = |S_{21}|^2$) can be determined. Finite Element simulations were performed for Al/SiO₂/Al structures shown in Fig. 3, using parameters listed in Table 1. The arrows (proportional plot) in Fig. 4(b) represent the anti-parallel surface currents excited in the two metallic layers in the metamaterial unit cell, while the surface colors represent the electric field magnitude. Notice that there is no transmission of the incident wave.

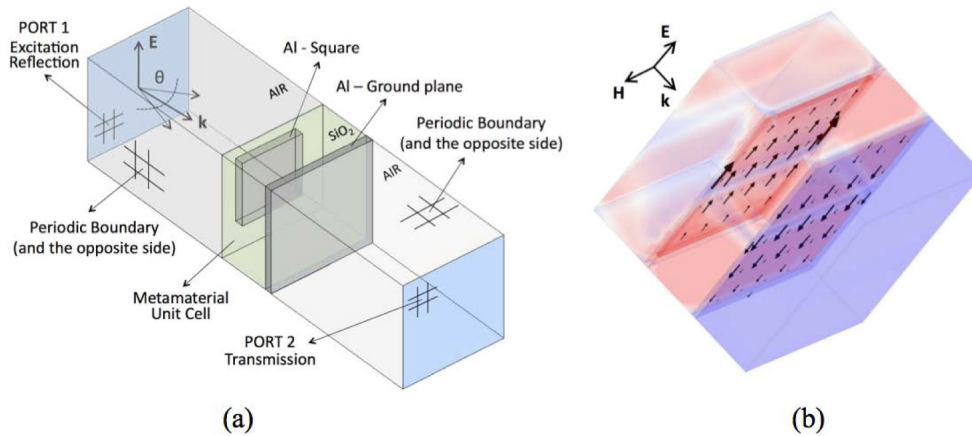


Fig. 4. Finite element modeling of a metamaterial unit cell using COMSOL Multiphysics RF module. (a) Unit cell simulation parameters. Two external ports and periodic boundary conditions allow the extraction of the S-parameters and consequently reflection and transmission. Integration of the resistive loss gives the absorbed energy in the unit cell. (b) The arrows (proportional plot) represent the anti-parallel surface currents excited in the two metallic layers in the metamaterial unit cell, while the surface colors represent the electric field magnitude. Notice that there is no transmission of the incident wave.

The absorption ($A = 1-R-T$) is the amount of power not reflected (R) and not transmitted (T) due to the negligible contribution of higher order scattering from the metamaterial structure in this study [43]. In addition, absorption can be obtained directly by integrating the resistive losses in the unit cell (surface plot in Fig. 5(a)). Since all the constitutive relations used in these models are assumed to be linear, it is convenient to set the radiation flux into the unit cell to 1 watt, allowing the total resistive losses to simply be read off as absorptance. An additional advantage of integrating resistive losses is that the contribution of individual layers can be examined separately for optimizing the detector design.

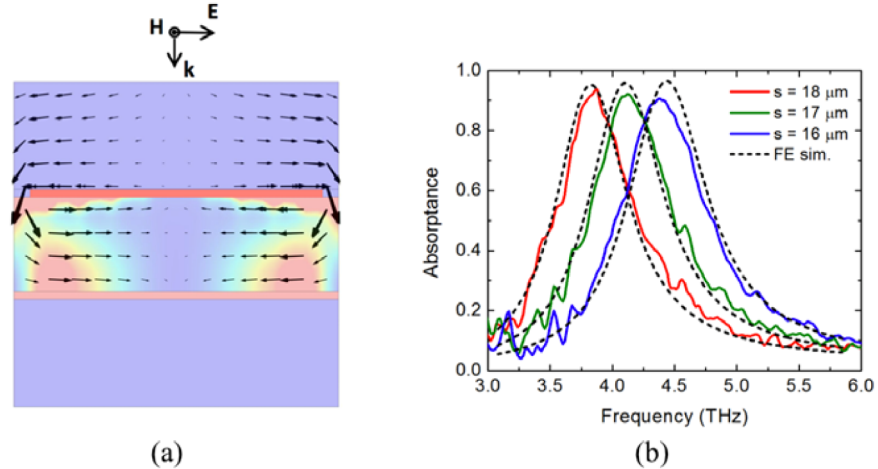


Fig. 5. Finite element simulations of a metamaterial unit cell using COMSOL Multiphysics RF module. (a) The surface colors represent the resistive loss in the structure where blue represents no loss. The arrows (proportional plot) represent the average power flow in the unit cell. Notice that there is no power transmitted. (b) Comparison between measurement (solid lines) and FE simulations (dashed lines) of absorbance of three metamaterial structures fabricated with the same repetition period ($20\ \mu\text{m}$) and different square sizes.

Figure 5(a) also shows the average power flux (arrows) where no observable flux is found below the metamaterial layer. This indicates that the ground plane is thicker than the skin depth of Al for the simulated frequency, which is a necessary to obtain absorption close to 100%.

A set of metamaterial absorbers consisting of different unit cell configurations was fabricated using Al/SiO_x/Al layers with standard microfabrication techniques. The details of the fabrication and their absorption characteristics are published elsewhere [27, 36]. Reflectance measurements were performed at 15° incidence using a Thermo-Nicolet Nexus 870 Fourier Transform Infrared Spectrometer (FTIR) with a global source fitted with a PIKE Technologies MappIR accessory. An aluminum-coated Si wafer was used to establish the background for the reflectance measurements. Since the ground plane prevents transmittance, the absorbance can be simplified to 1-R. Figure 5(b) shows the simulated and measured absorption spectra for 3 different structures with periodicity of $20\ \mu\text{m}$ and Al square sizes of 18, 17 and $16\ \mu\text{m}$. The approximate thickness for both the ground plane and square Al is about 100 nm while the SiO_x layer is $1.1\ \mu\text{m}$. The dimensions were selected to give peak absorption close to 3.8 THz, the frequency of the QCL available in our laboratory. It can be observed in Fig. 5(b) that the structure with square size of $18\ \mu\text{m}$ gives peak absorption around 3.8 THz and show absorption peak of 95%, making this configuration the best choice for the absorber to achieve maximum responsivity. The SiO_x and top Al layers can be used for making the bi-material legs, simplifying the fabrication process. Additionally, the Al ground plane is an efficient mirror for optical readout of deformation of pixel under THz absorption [8, 17, 18]. The square metamaterial geometry is particularly attractive since the difference in Al coverage on both surfaces of the central absorber is less than 20%. This helps compensate stress, making the mirror relatively flat, improving the efficiency of the optical readout.

5. Bi-material THz sensor design

Bi-material terahertz detectors were designed using a metamaterial structure optimized to absorb at 3.8 THz. Relatively large pixel dimensions were chosen to increase the absorption area and simplify the fabrication and characterization process. Thermal conductance was

intentionally varied among the designs while thermal capacitance remained essentially constant (see Table 2). Figure 6 shows the geometrical details of three sensors (A, B, and C) with different thermal conductances.

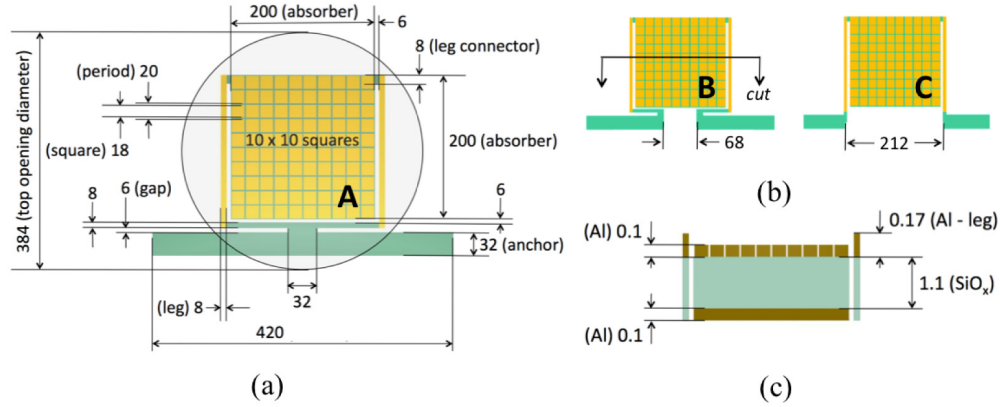


Fig. 6. Structural parameters of the three bi-material THz sensors. (a) Top view of sensor A showing all dimensions. (b) Top view of sensors B and C, showing the differences in sizes of the thermal insulator anchors. (c) Vertical cut of the sensor structure.

The detectors consist of a square metamaterial sensing element in the center connected to two symmetrically located rectangular bi-material legs. The entire structure is then connected to and thermally isolated from the substrate by folded SiO_x anchors with varied dimensions as shown in Fig. 6. The thickness of the Al ground plane and squares is 100 nm while the bi-material legs have a 170 nm layer of Al on the top side. The structural SiO_x is 1.1 μm thick everywhere. The thermal conductance (G) of all the sensors was estimated using the expression:

$$G = \frac{g_{th} A_C}{l}, \quad (4)$$

where g_{th} is the thermal conductivity, A_C is the cross-sectional area and l is the length. Since the dimensions of the thermal isolation sections are different, the total thermal conductance was estimated by adding the thermal resistance of each section. The metalized parts are considered thermal shorts due to their high thermal conductivity compared to that of SiO_x . The thermal conductance via radiation loss of heat is found to be an order of magnitude lower than that via the legs due to low emissivity of Al and the THz metamaterial that cover most of the sensor surfaces. Heat dissipation due to convection is negligible as the sensors typically operate under low pressure (in a vacuum chamber). The thermal capacitance was estimated using the expression:

$$C = c_{th} \rho A_s t, \quad (5)$$

where, c_{th} is the material thermal capacity, ρ is the material density, A_s is the surface area and t is the structure thickness. The thermal capacitance of the sensor is the sum of thermal capacitances of the SiO_x and Al layers. The material parameters used for the calculations are given in Table 1. The time constant ($\tau = C/G$) was also estimated for each sensor configuration and listed in Table 2 in addition to other parameters.

The deformation of the sensor with increasing temperature was analyzed using the COMSOL heat transfer module, which allows a uniformly distributed heat flux boundary to be placed at the absorber to emulate the incoming THz power. The anchor attachments to the substrate are fixed and set at constant temperature to represent the heat sink. All other boundaries are thermally insulated from the surroundings and free to move. The program

computes the heat transfer equation at each mesh point allowing the retrieval of several parameters, such as temperature distribution, thermal deformation, etc. For steady state simulations the total incoming heat flux was conveniently set as $1 \mu\text{W}$, therefore the thermal deformation and temperature distribution can be directly read “per unit μW ”. The angular deformation can be directly obtained by the displacement of the free edges of absorber and hence $d\theta/dT$ can be estimated using the temperature difference between the absorber and heat sink. Also, the responsivity ($d\theta/dP$) of the sensors can be obtained using the maximum deformation (steady state) and the incident heat flux ($1 \mu\text{W}$). Furthermore, thermal conductance can be estimated using Eq. (1). Time domain simulations were performed to obtain the transient response of the sensor to a pulsed heat flux allowing the retrieval of the time constant of the sensors. Using the obtained time constant and thermal conductance, we estimated the thermal capacitance of the sensors. The calculated and simulated parameters, using the material properties of Table 1, are listed in Table 2 and, in general, show good agreement. Notice that the thermal capacitance values obtained by FE simulations show a small discrepancy as they increase with decreasing sensor mass. This is most likely due to the time constant estimation, which is more susceptible to errors as it decreases. Figure 7(a) to 7(c) show the deformation plots obtained by FE simulation, where the z-axes are scaled up 20 times for visual purposes. The surface color scale indicates the temperature distribution and it is the same for all sensors. It can be seen in Fig. 7 that sensor A deflects more compared to sensors B and C under the same incident power ($1 \mu\text{W}$) primarily due to lower thermal conductance. Figure 7(d) shows the time domain simulations where the sensors are submitted to a step excitation (black solid line) of $1 \mu\text{W}$ for duration of 8 seconds. The vertical axes show temperature on the left side and angular deflection on the right side.

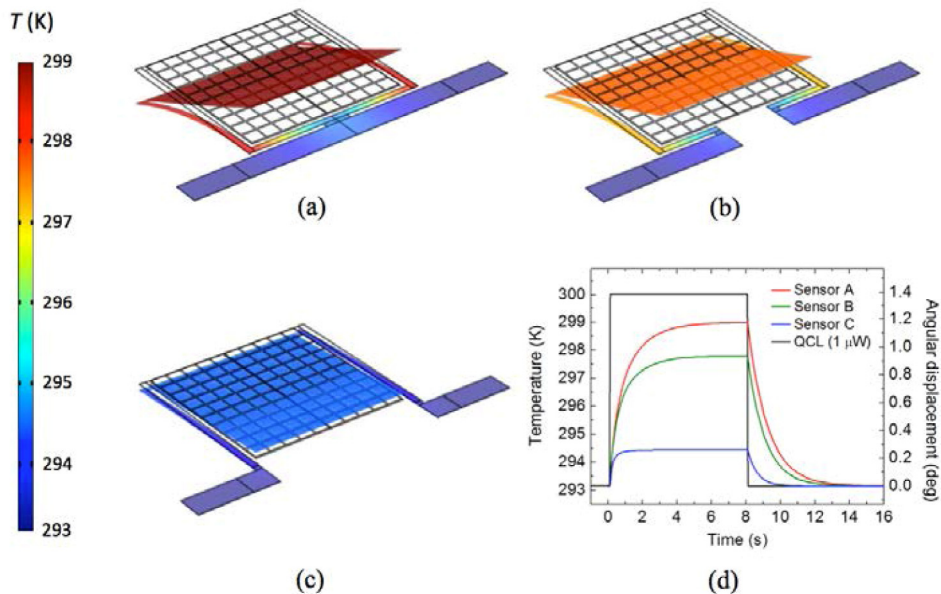


Fig. 7. FE simulations showing the deformation plots of sensor A (a), B (b) and C (c) under a constant $1 \mu\text{W}$ heat flux. The z-axes are scaled up 20 times for visual purposes. The surface colors indicate the temperature distribution according to the color bar on the left. (d) Time domain simulation of all three sensors under a $1 \mu\text{W}$ step excitation (black line). Temperature change and angular displacement are shown on the left and on the right, respectively.

Noise sources intrinsic to the detectors were also considered and an analysis similar to that in [31] was performed to determine the NEP. The expressions given by Eqs. (6) and (7) were adapted from [31] to reflect angular deflection fluctuations. The primary noise sources in

thermal detectors are temperature fluctuation, background fluctuation and thermomechanical noises. The spontaneous fluctuation in angular deflection (deg) of the absorbers caused by temperature fluctuations is given by

$$\langle \delta\theta_{TF}^2 \rangle^{1/2} = \frac{(d\theta/dP)T\sqrt{4k_BGB}}{\eta}, \quad (6)$$

where T is the sensor temperature, k_B is the Boltzmann constant, G is the total thermal conductance and B is the bandwidth, which can be set to unity. The background fluctuation noise can be obtained by replacing the total thermal conductance in Eq. (6) by thermal conductance via radiation loss of heat. However, this is much smaller than the thermal conductance via the legs and its contribution to noise can be neglected. The angular deflection (deg) due to thermomechanical noise, knowing that the detector operating frequency is much slower than the mechanical resonances (few kHz), is given by

$$\langle \delta\theta_{TM}^2 \rangle^{1/2} = \frac{360}{\pi l_b} \sqrt{\frac{4k_B TB}{Qk\omega_0}}, \quad (7)$$

where Q is the quality factor, k is the stiffness and ω_0 is the resonant angular frequency of the mechanical structure. Using the eigenfrequency solver in the COMSOL structural mechanics module, the first resonant frequency and stiffness of all the sensors were estimated and found to have values 3.5, 4.0 and 6.0 kHz and 0.02, 0.025 and 0.04 Nm^{-1} for sensors A, B and C respectively. Typical Q values for similar structures lie between 100 and 1000 in vacuum [31]. The noise was estimated and as expected, the dominant source is the temperature fluctuation in the detector. The total noise intrinsic to the sensors was estimated to be 5.0, 4.0 and 2.0 μdeg . The NEP values of the three sensors were calculated by dividing the fluctuations due to the noise by their respective responsivities, and are listed in Table 2.

6. Fabrication and characterization

The sensors were fabricated using standard micromachining technology. First, a 100 nm thick aluminum (Al) film was deposited on a 300 μm thick silicon (Si) substrate by e-beam evaporation. Then, the Al layer was patterned and wet etched to form the absorber ground plane. Next, a 1.1 μm thick SiO_x layer was deposited using plasma enhanced chemical vapor deposition (PECVD) at 300 $^\circ\text{C}$, followed by another 100 nm thick Al film. The second Al layer was then patterned and plasma etched to define the absorber metamaterial squares. Then a 170 nm thick Al layer was deposited, patterned and lifted off to form the bi-material legs. The sensor structure was then created by reactive ion etching of the SiO_x layer. Finally, the structures were released through backside trenching using the Bosch etch process. Circular openings were chosen to ensure release of the structure and to help refine the Bosch etch recipe. Figure 8(a) and 8(c) show the optical profile of the fabricated sensor A along with micrographs of the three sensors and an array of sensors of type A. The 3D profile in Fig. 8(a) is an actual view of sensor A while the 2D profile in Fig. 8(c), taken along the bi-material legs direction (y -profile), is exaggerated in the processing direction (z -profile) to show the residual deflection of the legs and absorber of the sensor. The measured residual deflection of the absorber is approximately 6° for the sensors A and B and 8° for sensor C. It is easy to observe that the absorber is almost flat due compensation of stresses from the aluminum layers in both sides of the SiO_x layer. Due to the deflection of the sensors, micrographs shown in Fig. 8(d) are not completely focused across the surface. In addition to the sensors, the fabricated wafer contains an area of $10 \times 10 \text{ mm}^2$ filled with the same metamaterial structure used in the sensors. This is to allow accurate measurement of the absorption characteristics of metamaterial used in the sensors.

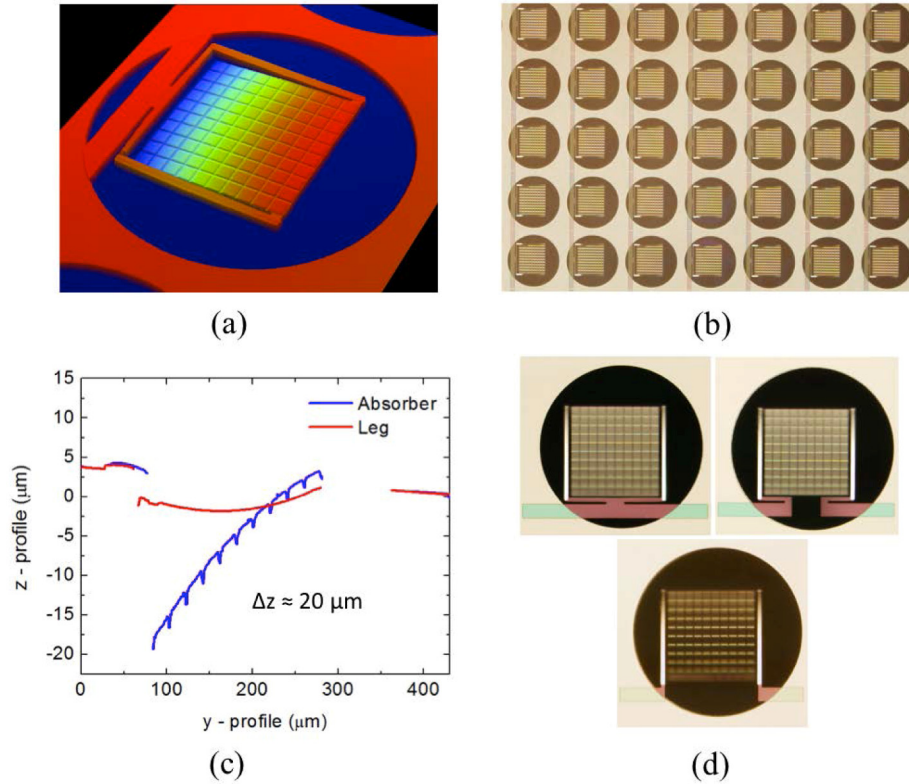


Fig. 8. Fabricated THz bi-material sensors. (a) 3D optical profile of sensor A (the aspect ratio is preserved). (b) Micrograph of an array of sensor A. (c) 2D profile taken along the bi-material legs direction (y-profile) with the processing direction (z-profile) scale exaggerated to show the residual deflection of the legs (red line) and absorber (blue line). (d) Micrographs showing the top view of sensors A, B and C.

Table 2. THz bi-material sensor analytical numerical and experimental parameters.

Sensor Property	Sensor A			Sensor B			Sensor C		
	Anal.	FE	Exp.	Anal.	FE	Exp.	Anal.	FE	Exp.
Absorptance η	–	0.96	0.95	–	0.96	0.95	–	0.96	0.95
Thermal Conductance G ($\times 10^{-7} W K^{-1}$)	1.6	1.7	–	2.2	2.1	–	9.3	8.5	–
Thermal Capacitance C ($\times 10^{-8} J K^{-1}$)	11.1	12	–	10.7	12.5	–	9.8	11.9	–
Time constant τ (s)	0.68	0.7	0.8	0.47	0.6	0.5	0.1	0.14	0.3
Thermomechanical Sensitivity $d\theta/dT$ (deg K^{-1})	0.15	0.19	0.2	0.15	0.2	0.2	0.15	0.2	0.2
Responsivity $d\theta/dP$ ($\times 10^6$ deg W^{-1})	0.95	1.1	1.2	0.65	0.9	0.8	0.15	0.25	0.2
Noise Equivalent Power (due to incident power) NEP ($\times 10^{-9} W$)	0.005	–	8.6	0.006	–	13	0.014	–	45

The absorptance of the metamaterial film was measured as described in section 4 and compared with the QCL emission characteristics as shown in Fig. 9(a). A good match between the absorptance peak position of the metamaterial and the 3.8 THz QCL emission frequency was achieved with nearly 95% absorptance. This assured that the sensors absorbed our QCL emission with high efficiency.

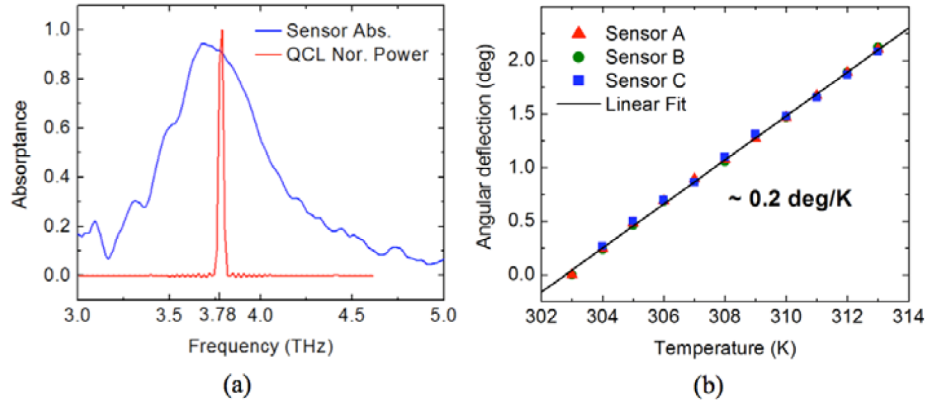


Fig. 9. (a) Measurement of the absorptance spectra of the THz sensors metamaterial structure (blue line) compared with the QCL normalized emission (red line). (b) Measured angular deflection (markers) upon temperature change. Notice that the effect is linear and almost indistinguishable among the sensors, resulting in approximately 0.2 deg/K thermomechanical sensitivity.

Next, the thermal response of the sensor ($d\theta/dT$) was measured. The temperature gradient in the bi-material section of the leg was estimated to be less than 5% of that between the central absorbing element and the substrate. Thus, the bi-material section of the leg can be treated as thermally shorted allowing the measurement of the thermal response by uniformly heating the sensor. The measurement was performed by attaching the sensor to a flat resistive heating element and sweeping the temperature from 303 to 313 K. The reflection of a laser diode beam from the backside of the sensor's ground plane was projected on a screen and the angular deflection of the sensor was determined. Angular deflections from the three sensors are shown in Fig. 9(b) with different markers. The deflections are almost indistinguishable because the detectors have the same bi-material leg dimensions. The solid line is a linear fit, showing that the response in this temperature range is linear and approximately 0.2 deg/K, which is slightly higher than the estimated values (see Table 2 and Fig. 2). Figure 2 shows that the thermal response of the sensors can be further increased by, for example, decreasing the SiO_x thickness or increasing the Al thickness on the legs. Test structures fabricated in parallel with these sensors showed that increasing the Al thickness on the legs also increases the residual stress. Decreasing the dielectric thickness has a similar effect in addition to reducing absorber efficiency [27]. Further tuning of the fabrication process is necessary to reduce the residual stress on the bi-material legs to decrease the initial bending as depicted in Fig. 8(a).

Subsequently, the sensors were placed in a vacuum chamber and operated at a pressure of approximately 0.03 mTorr to minimize the heat loss by convection [29]. The QCL was kept inside a cryostat and operated at around 15 K. The divergent THz beam passed through the cryostat Tsurupica window and the radiation was focused by a 40 mm polyethylene lens onto the sensors. Both Tsurupica and polyethylene exhibit reasonable transmission ($\sim 65\%$) in the THz range. The QCL was operated in pulsed mode with the pulse width fixed at 5 μs and a variable pulse rate to control the output power. The deflection of the sensor was measured using the same procedure described earlier for a set of QCL pulse rates ranging from nearly zero to 5 kHz. The absolute power that reaches the sensors (incident power) is estimated

using the responsivity ($d\theta/dP$) in Eq. (2) along with the calculated thermal conductance and measured absorptance. Note that the QCL switching frequency and duty factor must be taken into account since the sensors can only respond to the average power. Figure 10(a) shows the measured angular deflection versus incident power for all three sensors (colored markers). For all of the sensors, the responsivity values estimated analytically tend to be lower than that of the FE and experimental values mainly due to the underestimation of bimetallic effect ($d\theta/dT$), by Eq. (3) (see Fig. 2). As expected from Eq. (2), responsivity of the sensors was found to decrease with increasing thermal conductance.

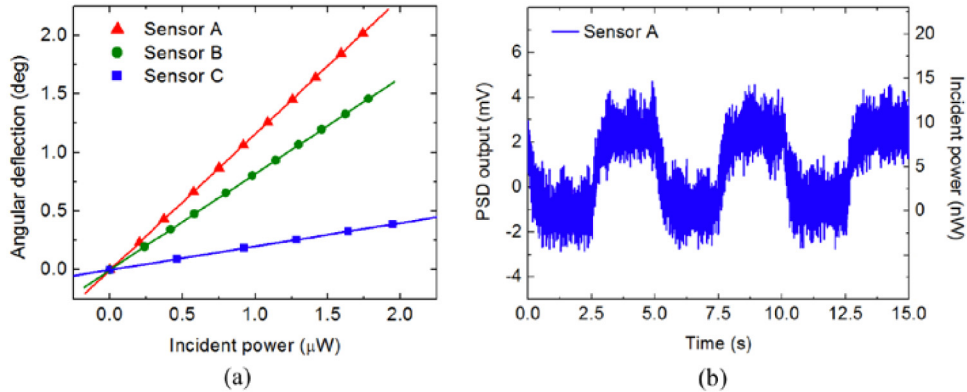


Fig. 10. Responsivity and NEP measurements. (a) Measured angular deflection per varying incident power for all three sensors (colored markers) Notice that responsivity increases as thermal conductance decreases. (b) Measured output voltage of the PSD for sensor A by gating the QCL output at 200 mHz. The power incident in the detector is shown on the right vertical axis.

To determine NEP, a position-sensing detector (PSD) was added to the experimental setup to read the deflection at low power levels. The NEP was then measured for each detector and listed in Table 2. Figure 10(b) shows measured output voltage of the PSD for sensor A by gating the QCL output at 200 mHz. It is important to highlight that the measurements include the effects of QCL power fluctuations and optical readout noise, not considered in the theoretical estimations discussed earlier. The difference between the measured values (3 orders of magnitude higher) and the estimated ones (Table 2) can be attributed primarily to the readout noise. The QCL power fluctuations [44] do not seem to contribute to the observed noise since the noise floor when the QCL is off, shown in Fig. 10(b), is similar to the noise observed when the QCL is on. As expected, NEP increases from sensor A to C due to decrease in responsivity. The measured NEP values, including the readout noise and the intrinsic noise of the sensor, can be translated into minimum detectable temperature difference on the sensor, found to be approximately 50 mK for all three sensors. This value is similar to those of bi-material sensors operating in the IR range [8, 31].

The time domain response was also measured using the PSD and the results for the three sensors are shown in Fig. 11(a) under the same incident power with the QCL gated at 500 mHz. As observed in Fig. 11, sensor A is more sensitive, which agrees with the predictions and previous measurements. Since the sensors have the same η , the same absorbing area, same materials, the same $d\theta/dT$, and nearly the same thermal capacitance, speed and responsivity are completely controlled by the thermal conductance, which depends on the anchor geometry.

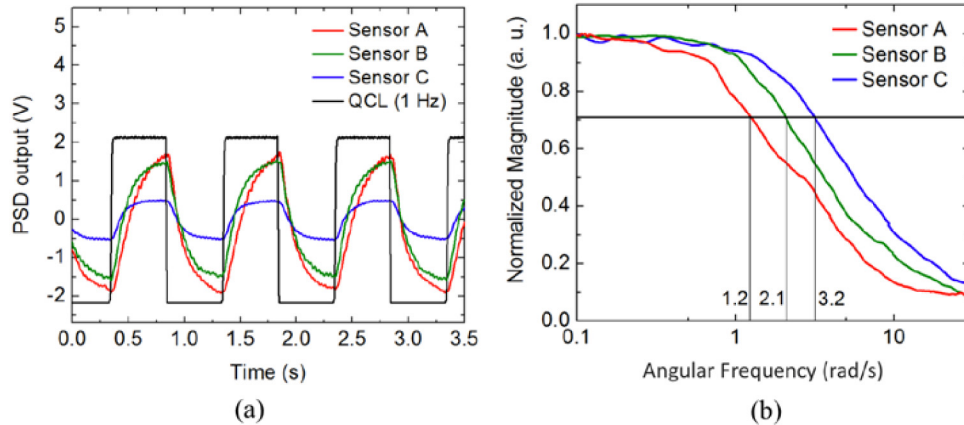


Fig. 11. Time and frequency domain measurements. (a) Time responses of sensors A, B and C measured under the same incident power with the QCL gated at 1 Hz. Noticed that sensor A is more sensitive and slower, which agrees with the predictions and previous measurements. (b) Normalized frequency responses for the three sensors (colored lines). The time constants were retrieved by taking the inverse of the 3 dB frequencies that are 1.2, 2.1 and 3.2 rad/s for sensor A, B and C respectively.

The time constant of the sensors was determined by sweeping the QCL gating frequency from 50 mHz to 30 Hz and recording the PSD peak to peak voltage. The normalized frequency responses for the three sensors are shown in Fig. 11(b). The time constants were retrieved from Fig. 11(b) by taking the inverse of the 3 dB frequency and included in Table 2. In general, the measured time constants agree well with the FE estimations, while the analytical approach underestimates this parameter. The sensors are, apparently, slow for real time imaging; however, pixel size can be reduced to increase the speed of operation. A tradeoff between speed and sensitivity has to be made according to specific applications. Although the fabricated sensor arrays do not have high spatial resolution, their imaging capabilities were probed by a CCD camera with coaxial illumination as schematically illustrated in Fig. 12(a) [17, 18]. A real time video recording of the QCL beam, gated at 500 mHz, is shown in Fig. 12(c) ([Media 1](#)) compared with the same image obtained using a commercial IR microbolometer camera with THz optics [7] (Fig. 12(b)). The focal plane array of the IR camera has 30 μm pitch of and can resolve the rings associated with the QCL beam. Our sensor array, on the other hand, has a 430 μm pitch and cannot resolve the rings; nevertheless, it gives a raw image that clearly shows where the energy is concentrated and the circular shape of the THz beam. Figure 12(d) ([Media 2](#)) shows the deflection of sensor A when excited by the QCL gated at 500 mHz. Finally, it is possible to optimize THz bi-material sensor configuration, size, fabrication processes and readout to achieve real time imaging.

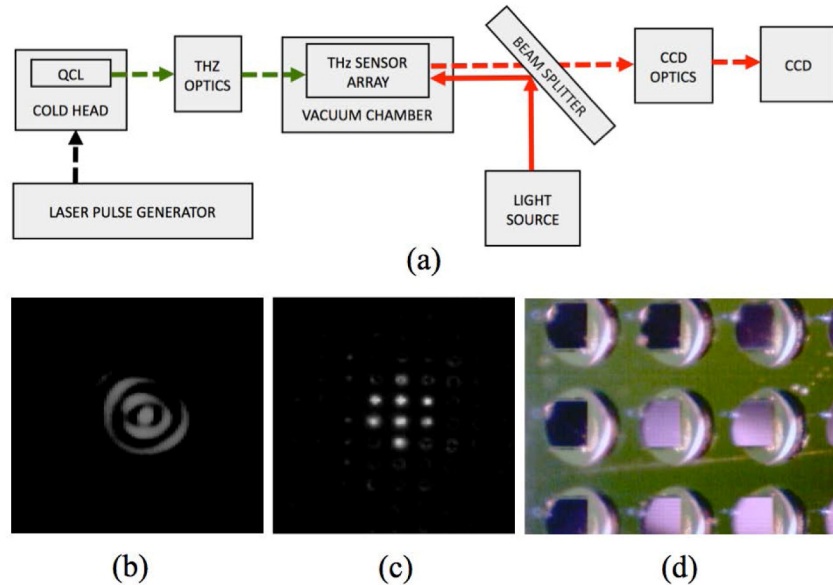


Fig. 12. QCL beam imaging. (a) Optical readout used to record videos [46] and the snap shot showed in part (c). The images were recorded using background subtraction to suppress to the effects of the residual stress of the sensors. (b) Image obtained using a $30\ \mu\text{m}$ pitch commercial IR microbolometer camera with THz optics. (c) Image (Media 1) of the same QCL beam, gated at 500 mHz, obtained using an array of sensor A with $430\ \mu\text{m}$ pitch using the readout depicted in part (a). Notice that since the pitch of our sensor are one order of magnitude higher than the IR camera, it cannot resolve the rings associated with the QCL beam, showed in part (b). (d) Close up of sensor A (Media 2) moving due to THz absorption of a QCL beam, gated at 500 mHz.

7. Conclusion

In summary we have demonstrated the design, fabrication and characterization of bi-material MEMS sensors, using metamaterial absorbers operating in THz range. Sensor materials and configurations were chosen in order to maximize responsivity. The combination of favorable thermal, mechanical and optical properties of the MEMS fabrication-friendly materials SiO_x and Al were advantageous. Analytical and FE models were used to predict the performance of the sensors. A highly efficient metamaterial structure was developed to provide near 100% absorption at 3.8 THz, while simultaneously serving as a structural layer and providing access for external optical readout. The fabricated sensors showed responsivity values as high as $1.2\ \text{deg}/\mu\text{W}$ and time constants as low as 200 ms, depending on the configuration. Minimum detectable power on the order of 10 nW was observed, demonstrating that the sensors can operate with low-power THz sources. Although the sensors were not optimized for imaging, the use of an external optical readout allowed us to obtain raw images of the QCL beam indicating the potential of these detectors to be further optimized for use in focal plane arrays for real time THz imaging.

Acknowledgments

This work is supported in part by grants from the ONR and NRO. The authors would like to thank John Dunec, Emmanuel Dupont, Elison Montagner, Mun Wai Raymond and Sam Barone for technical assistance. A portion of this research was conducted at the Center for Nanophase Materials Sciences, which is sponsored at Oak Ridge National Laboratory by the Scientific User Facilities Division, Office of Basic Energy Sciences, U.S. Department of Energy.